Configurational Aspects of a Circulation Controlled High-Lift System for a Medium-Haul Transport Aircraft

Dennis Keller* and Ralf Rudnik*

*Institut für Aerodynamik und Strömungstechnik,, Deutsches Zentrum für Luft- und Raumfahrt,, Lilienthalplatz 7, 38108 Braunschweig

Abstract

Configurational aspects concerning the aerodynamics of a high-lift system with circulation control are investigated based on numerical investigations of two transport aircraft concepts. The two investigated concepts mainly differ in their engine type and position, vertical wing position, and wing sweep. The comparison of the two concepts indicate that all three aspects have a notable influence on the lift generation in landing configuration. A high wing position as well as an engine mounted in front of the main wing are both more favorable than a low wing position and an engine located behind the main wing in landing configuration. The wing sweep affects the lift generation as well as the stall behavior. The wing stall of the configuration with high positive wing sweep occurs due to flow separation in the outboard region, whereas the main wing of the configuration with low positive wing sweep stalls due to flow separation in the inboard region. The concept with engines mounted above the main wing trailing edge was furthermore investigated for intake flow distortion. While the landing configuration is uncritical concerning this matter, the take-off configuration reveals increasingly distorted intake flow with rising angle of attack.

Nomenclature

Roman Symbols

$\dot{m}_{\text{jet}}$	jet mass flow rate,	kg/s
b	wing span, m	
c_{ref}	mean aerodynamic chord,	m
C_μ	jet momentum coefficient $\frac{\dot{m}_{\text{jet}} V_{\text{jet}}}{q_\infty S_{\text{ref}}}$	
C_p	Pressure coefficient, $\frac{p-p_\infty}{q_\infty}$	
C_L	aircraft lift coefficient $\frac{L}{q_\infty S_{\text{ref}}}$	
C_T	thrust coefficient $\frac{T}{q_\infty S_{\text{ref}}}$	
L	lift force,	N
M	Mach number	
p	pressure,	Pa
p_t	total pressure,	Pa
$p_{t,\infty}$	free stream total pressure,	Pa
q	dynamic pressure $\frac{\rho V^2}{2}$,	Pa
S	surface area	
T	thrust,	N
V_∞	reference velocity,	m/s
X	roll axis	

doi:10.25967/490128

Y	pitch axis	
Z	yaw axis	

Greek Symbols

α	angle of attack,	deg
δ_{Flap}	flap deflection,	deg
η	dimensionless spanwise coordinate $\frac{2Y}{b}$	
Φ	wing sweep angle,	deg
ρ	density,	kg/m^3
Θ	wing twist angle,	deg

1 Introduction

In the context of the Collaborative Research Center CRC 880, technologies related to short take-off and landing (STOL) capabilities are investigated based on several novel low noise commuter aircraft designs. The STOL capabilities potentially allow to save emissions and travel time by utilizing existing aerospace infrastructure more efficiently. In order to allow for short runway usage, an active high-lift system utilizing circulation control (CC) is employed. The potential of such systems is already well known [1, 2, 3, 4] and is further assessed within the research project. The actual performance depends on the system's integration into the aircraft and therefore has to be assessed as such. For this purpose, the CRC 880 investigates several aircraft concepts of which two are compared in the present study. The REF2-2013 is a high wing configuration with a leading edge wing sweep of $\Phi = 10°$. It is equipped with two turbo-prop engines designed for a cruise Mach number of $M_{cr} = 0.74$. The aerodynamic behavior of the REF2-2013 landing configuration has been thoroughly studied in previous investigations [5, 6, 7, 8]. Considering slipstream effects, the REF2-2013 achieves a maximum lift coefficient of $C_{L,max} = 4.5$ in landing configuration. REF3-2015 is a low wing configuration with a higher cruise Mach number of $M_{cr} = 0.78$. It therefore has a higher leading edge wing sweep of $\Phi = 26°$. The aircraft is powered by two UHBR turbofan engines mounted over the wing, aft of the trailing edge. Preliminary investigations of the REF3-2015 landing configuration with a reduced chord flap yielded a maximum lift coefficient of $C_{L,max} = 2.75$ [9].

The present study focuses on the configurational influences on the aerodynamics of a circulation controlled high-lift system by comparing the numerical results of the landing configurations of the transport aircraft concepts described above. The basic aerodynamic behavior of the two concepts in landing configuration is first discussed. Then the influence of the main configurational differences between the two concepts on the aerodynamic behavior in landing configuration is analyzed. Furthermore, the present study provides an overview on the aerodynamic performance of the REF3-2015 take-off configuration and assesses the possibility of flow distortion at the engine intake of the REF3-2015 high-lift configurations.

2 Numerical methods

The calculations are performed with the *DLR TAU* code [10], which is based on an unstructured finite volume approach for solving the Reynolds-averaged Navier Stokes equations. For this investigation, the implicit LU-SGS scheme is used for time stepping and a central scheme and second order Roe upwind scheme for the spatial discretization of the inviscid mean flow fluxes and the turbulent convective fluxes, respectively. The turbulence effects are modeled with the Spalart-Allmaras formulation (SA) [11] with vortical and rotational flow correction based on the Spalart-Shur correction [12]. The rotational correction improves vortex modeling compared to basic one- and two-equation turbulence models [13], as it reduces excessive eddy viscosity within the vortex cores. The used numerical setup, in particular the turbulence model with rotational and curvature correction, has already shown good results in comparison with wind tunnel experiments for this type of simulations in previous studies [14, 15].

3 Geometric model

The basis of the investigation are two generic medium-haul transport aircraft concepts (REF2-2013 and REF3-2015), which were both designed with the preliminary aircraft design tool PrADO [16] in the course of the CRC 880. At maximum payload corresponding to 100 passengers, the mission range of both concepts is around 2000 km. One of the main difference in the top level aircraft requirements between the two concepts is the cruise Mach number. With REF3-2015's cruise Mach number being $M_{cr} = 0.78$, it is higher compared to REF2-2013's cruise Mach number of $M_{cr} = 0.74$. The variation in the cruise speed results in some key differences in the aircraft design. Firstly, the REF2-2013's leading edge wing sweep is rather low with $\Phi_{LE} = 10°$, whereas the REF3-2015 has a leading edge wing sweep of $\Phi_{LE} = 26°$. Secondly, REF2-2013 is powered by two turbo-prop engines mounted in front of the wing. In contrast the propulsion system of REF3-2015 consists of two ultra-high bypass ratio (UHBR) turbofan engines located over the main wing's trailing edge at 31% half span. The UHBR engine was designed by the Institute of Jet Propulsion and Turbomachinery (IFAS) of the Technical University of Braunschweig [17]. Since the main landing gear is retracted into the engine pylon, the pylon size of the REF3-2015 is larger compared to typical engine pylon sizes.

In order to account for the engine set-up, REF2-2013 has a high wing position whereas REF3-2015's wing position is at the lower side of the fuselage. The wing twist differs only slightly between the two concepts. Early results on the high-lift performance of the REF2-2013's predecessor REF0-2011 indicated premature flow separation at the outboard wing in landing configuration [18]. The wing twist of REF2-2013, which was originally chosen based on cruise performance critera, was therefore modified in order to prevent outboard flow separation in landing configuration. The twist was set to $\Theta = 0°$ in the wing root section with a linear decrease to $\Theta = -7°$ at the wing tip. For REF3-2015, the wing twist values at the wing root and the wing tip have been adopted from REF2-2013. However, the distribution along the span differs with the twist being zero for the entire inboard region ($\eta \leq 0.34$) and then progressively decreasing to $\Theta = -7°$ at the wing tip. The modification was introduced to account for the varying propulsion system and the resulting absence of slipstream effects. Further aircraft parameters of the two concepts are summarized in table 1.

	REF2-2013	REF3-2015
Reference area	95m^2	99m^2
Span	28.783m	28.745m
Aspect ratio	9.00	8.346
Sweep angle (leading edge)	10°	26°
Mean aerodynamic chord	3.428m	3.805m
Propeller diameter	5m	-
Nacelle diameter	-	2.29m
Engine bypass ratio	-	17
Maximum thrust	2 x 88 kN	2 x 134 kN

Table 1: Basic aircraft parameters of the REF2-2013 and REF3-2015 configuration

3.1 High-Lift System

Both aircraft designs are equipped with the same type of high-lift system consisting of a droop nose and internally blown plain flaps and ailerons. Blowing is realized by the integration of a high-pressure plenum into the main wing above the flap kink, which is located at a relative chord length of $c_{\text{Flap}}/c = 0.75$ (Fig. 1). The design of the blowing slot is based on previous investigations done by the Institute of Fluid Mechanics of the Technical University of Braunschweig [3]. For optimal efficiency of the circulation control, the plenum along the wing span is separated into six sections, which can be independently pressurized to adjust the blowing to the local flow conditions [18]. The total pressure within the plena was tuned to obtain fully attached flaps and ailerons at the smallest possible amount of blowing, resulting in the critical jet momentum coefficient.

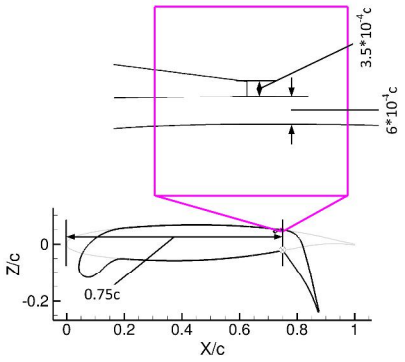

Figure 1: Main wing section with slot geometry

Due to the very high effective camber, the position of the leading edge stagnation line is shifted far towards the rear. In order to circumvent leading edge separation, the aircraft is equipped with a flexible droop nose. The droop nose has also been designed by the Institute of Fluid Mechanics of the Technical University of Braunschweig [19]. The REF2-2013 and REF3-2015 models in landing configuration are depicted in figure 2 and 3, respectively. The main parameters of the high-lift devices in take-off and landing configuration are summarized in table 2. The general similarity of the two landing configurations is demonstrated in figure 4.

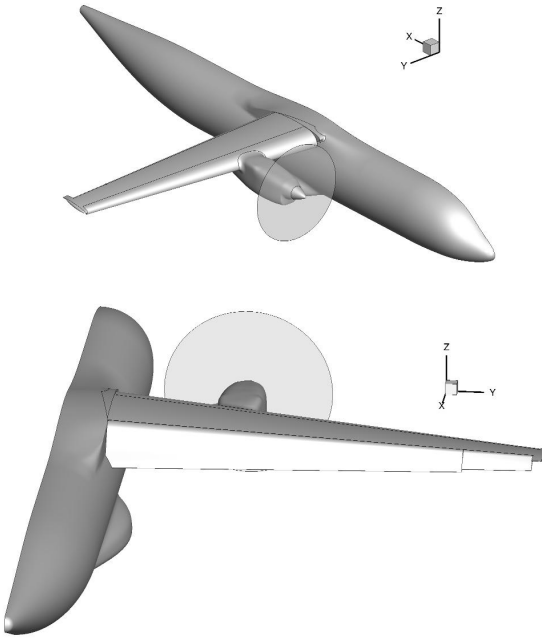

Figure 2: Overview of the REF2-2013 landing configuration

	Take-Off conf.	Landing conf.
Droop nose deflection	41.8°	41.8°
Flap deflection	45°	65°
Aileron droop	30°	45°

Table 2: Basic settings of the REF2-2013 and REF3-2015 high-lift configurations

Several meshing studies have been performed for a wing section of the 3D configuration prior to the present investigation [18]. Within these studies, different mesh topologies of structured meshes and unstructured meshes were investigated. For both mesh types, mesh convergence studies were conducted. The mesh of the REF2-2013 landing configuration has been built on the basis of these studies. It was created with a semi-automated hybrid meshing approach using the Centaur mesh generator [20]. Centaur first creates a surface grid based on triangles and quads. From the surface grid, a near-field volume mesh is generated with an advancing-layer algorithm. Due to the characteristics of the surface mesh, the near-field mesh consists of prism and hexahedra stacks. Outside of the near-field mesh, the computational domain is filled with tetrahedra. Figure 5 depicts the surface mesh (consisting of 1.1 million surface grid points) at the droop nose and in the region of the blowing slot. The figure shows that the surface mesh is triangle-dominated. The near-field mesh consists of up to 39 layers grown with a stretching ratio of 1.27 and first cell heights varying between $5 \cdot 10^{-7} m$ in the plena and $5 \cdot 10^{-6} m$ on the fuselage. The volume mesh size is 47 million points. More de-

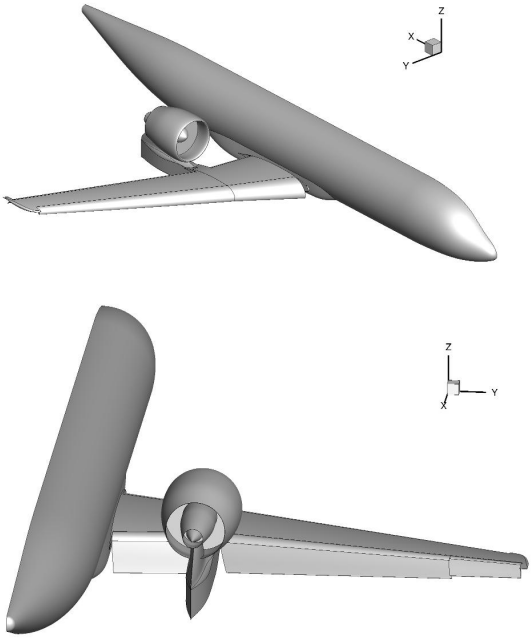

Figure 3: Overview of the REF3-2015 landing configuration

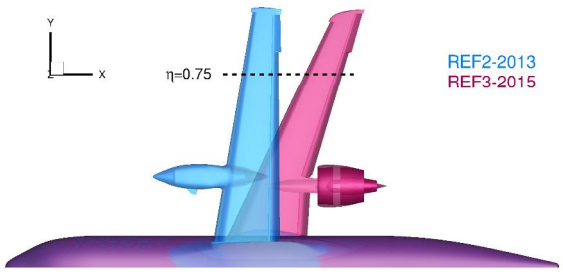

Figure 4: Geometry comparison of REF2-2013 and REF3-2015 landing configuration

tails regarding the meshing approach in particular of the slot region can be found in previous publications [18, 5, 6].

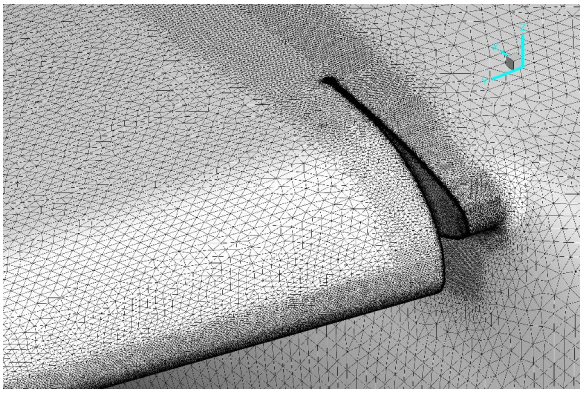

(a) Wing-body junction at the main wing leading edge

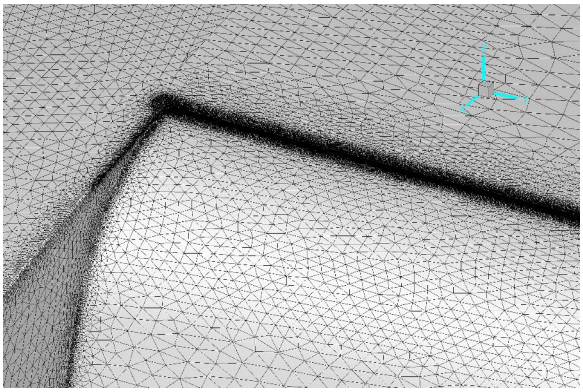

(b) Outboard trailing-edge flap and slot region at the wing-body junction

Figure 5: Close-up view of the surface mesh of REF2-2013 in landing configuration

The computational meshes for the REF3-2015 configurations have been built using the SOLAR grid generation software, which was originally developed by ARA, QinetiQ, BAE Systems, and Airbus [21, 22]. Similar to Centaur, SOLAR first creates a surface grid, from which an advancing-layer volume mesh is grown. Outside of the near-field mesh, the computational domain is again filled with tetrahedra. The surface meshes of the REF3-2015 take-off and landing configuration each consist of 3.1 million surface grid points. As shown in figure 6, the surface mesh is quad-dominated. The near-field mesh therefore mainly consists of hexahedra-stacks. The first cell

height is $10^{-6}m$ and the stretching ratio in normal direction of the near-field mesh is set to 1.22. The settings result in a volume mesh size of 140 million grid points for both high-lift configurations.

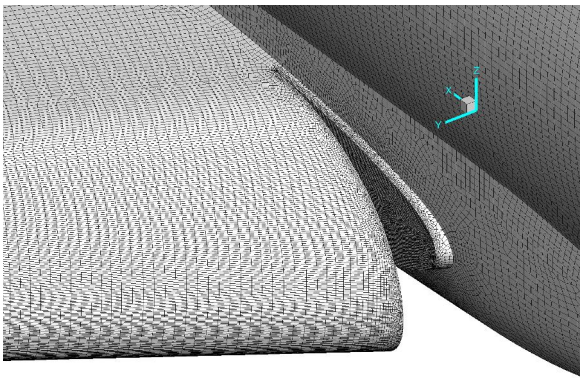

(a) Wing-body junction at the main wing leading edge

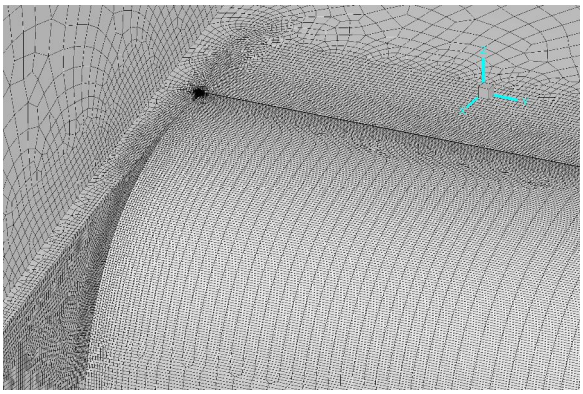

(b) Outboard trailing-edge flap and slot region at the wing-pylon junction

Figure 6: Close-up view of the surface mesh in landing configuration

4 Results

The high-lift configurations of REF2-2013 and REF3-2015 have been evaluated under slightly different conditions as summarized in table 3. The REF2-2013 take-off configuration has not been investigated. As the aerodynamic behavior of the REF2-2013 landing configuration is highly dependent on the thrust setting, computations with and without thrust have been carried out. With thrust, the propeller turns in inboard up direction and thrust is set to a thrust coefficient of $C_T = 0.54$ for a balanced flight at a glide slope of $\gamma = -3°$ at $\alpha = 6°$. The influence of thrust has not been investigated for the REF3-2015 high-lift configurations, yet. It is however expected that it has a minor influence.

	REF2-2013	REF3-2015
Altitude	$15m$	$15m$
Free stream Mach number	0.15	0.168
Reynolds number	$12.0 \cdot 10^6$	$14.9 \cdot 10^6$
Jet momentum coefficient (T/O)	-	0.013
Jet momentum coefficient (LDG)	0.031	0.021
Thrust coefficient (T/O)	-	1.14
Thrust coefficient (LDG)	0.54	0.25

Table 3: Flow conditions for high-lift computations of REF2-2013 and REF3-2015

4.1 REF2-2013 Landing Configuration

Figure 7 depicts the surface pressure distribution and skin friction lines of the REF2-2013 landing configuration without thrust. At a moderate angle of attack of $\alpha = 6°$, the skin friction lines indicate that the flow is fully attached to the main wing (figure 7(a)). However, the boundary layer flow behind the nacelle is disturbed due to nacelle vortices. The distribution of the surface pressure coefficient reveals suction peaks along the droop nose and the trailing edge devices, with the latter being stronger. At $\alpha = 14°$ (figure 7(b)), the skin friction lines still indicate fully attached flow. Nevertheless, the suction peak along the trailing edge flap is strongly reduced at the position of the nacelle vortices. The nacelle vortices cause

a wake burst [1], which in turn locally reduces the effectivity of the trailing edge flap. This phenomena limits the maximum lift of the configuration [7]. The complete lift break down then occurs due to leading edge separation in the inboard region.

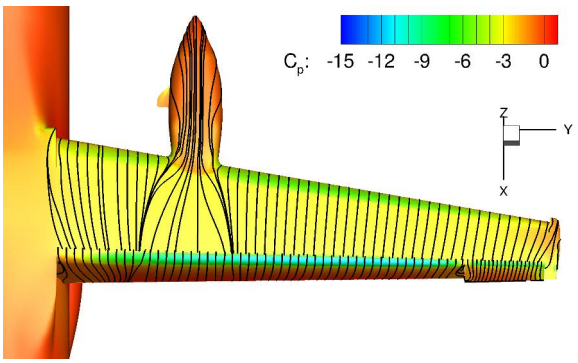

(a) $\alpha = 6°$

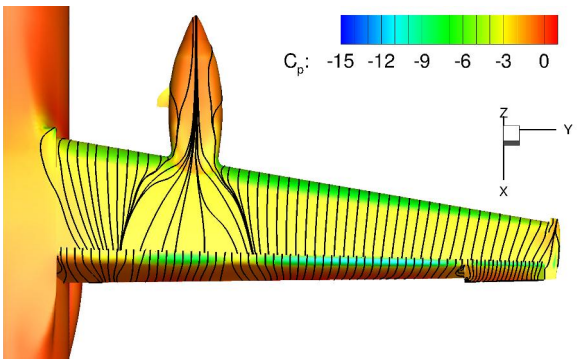

(b) $\alpha = 14°$

Figure 7: Surface pressure distribution and skin friction lines of REF2-2013 landing configuration without thrust at $C_\mu = 0.031$

When thrust is applied, the surface pressure distribution and skin friction lines are strongly affected by the propeller slipstream. At $\alpha = 6°$ (figure 8(a)), the skin friction lines indicate flow separation at the trailing edge flap behind the propeller. Nevertheless, the suction peaks at the leading edge and the trailing edge are notably increased in this region due to the velocity increase caused by the slipstream. In contrast to the case without thrust, the impact of the nacelle vortices cannot be observed. Instead, the skin friction lines indicate a spreading of the slipstream on the downwash side of the propeller, which is caused by the flow deflection due to the main wing. At $\alpha = 21°$ (figure 8(b)), leading edge separation occurs in the inboard region causing the lift breakdown of this configuration. Further details on the influence of propeller slipstream on a circulation controlled wing can be found in [5].

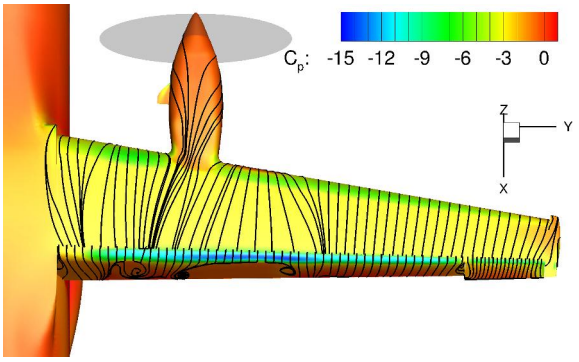

(a) $\alpha = 6°$

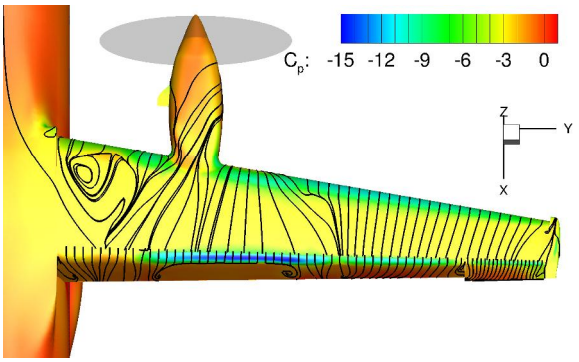

(b) $\alpha = 21°$

Figure 8: Surface pressure distribution and skin friction lines of REF2-2013 landing configuration with thrust at $C_\mu = 0.031$

[1] The wake from the main element of the wing separates from the circulation control jet above the flap.

4.2 REF3-2015 Landing Configuration

Figure 9 illustrates the surface pressure distribution and skin friction lines for the landing configuration of REF3-2015 at varying angles of attack.

At $\alpha = 6°$ (figure 9(a)), the flow is fully attached to the main wing and the trailing edge devices as demonstrated by the skin friction lines. The skin friction lines also indicate two vortices with one arising at the inner end of the droop nose and the other one at the outer end. The direction of the lines reveal that the inner vortex has a positive rotational sense, whereas the outer vortex is turning in the opposite direction. Flow field analysis indicates that both vortices are induced by the side-edges of the unprotected leading edge. Figure 10 shows the resulting total pressure losses due to the outer side-edge vortex at $\alpha = 6°$.

The surface pressure distribution indicates suction peaks along the droop nose and the trailing edge devices similar to the ones seen for the REF2-2013 landing configuration (see figure 7(a)). The suction peak at the leading edge however appears to be significantly degraded in the inboard region. The skin friction lines and the C_p-distribution on the nacelle indicate attached flow and rather high surface pressure on the upper side of the nacelle.

For a more detailed analysis of the nacelle's surface pressure distribution, figure 11 compares its chordwise C_p distribution at three different spanwise positions. The figure demonstrates lower pressure coefficients on the lower side of the nacelle compared to the upper side for $X \leq 18.2m$. At the rear of the nacelle, the surface pressure coefficient is lower on the upper side. The notable leading edge suction peak on the lower side, in particular at the inboard side, suggests that the nacelle is exposed to significant downwash from the main wing.

At $\alpha = 16°$ (figure 9(b)), the suction peak on the droop nose is notably increased compared to $\alpha = 6°$, whereas it is slightly reduced along the flaps. At the outboard wing, the side-edge vortex causes flow separation on the main element and the aileron as illustrated in figure 12. The suction peak on the aileron is therefore significantly deteriorated. Increasing the angle of attack further leads to a propagation of the flow separation towards the midboard region as seen for $\alpha = 18°$ (figure 9(c)).

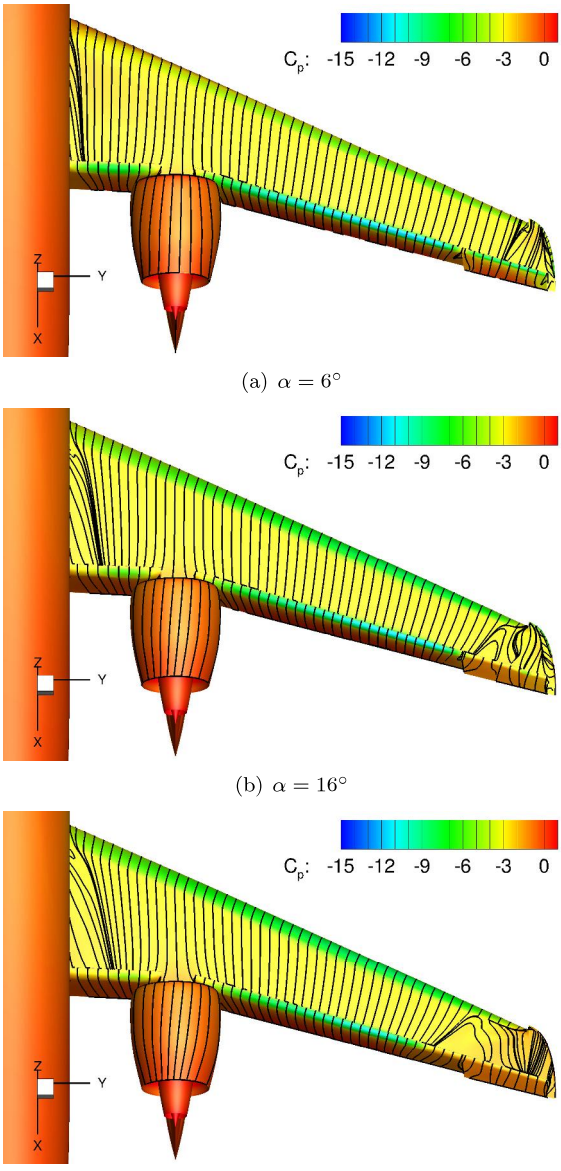

(a) $\alpha = 6°$

(b) $\alpha = 16°$

(c) $\alpha = 19°$

Figure 9: Surface pressure distribution and skin friction lines of landing configuration at $C_\mu = 0.021$

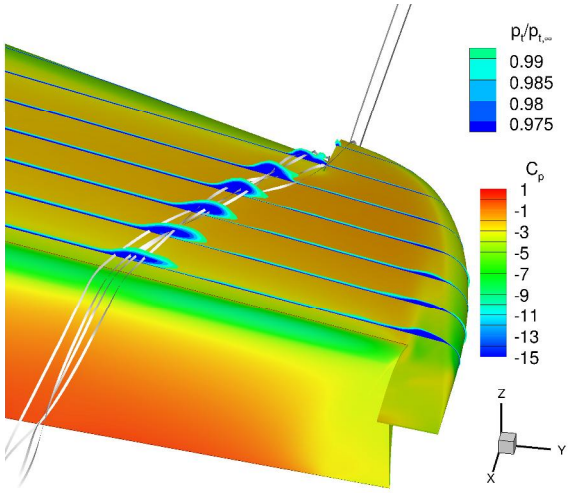

Figure 10: Total pressure loss due to side-edge vortex at the outboard wing ($\alpha = 6°$)

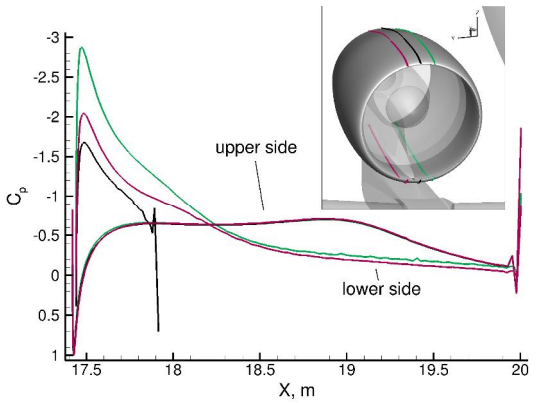

Figure 11: Surface pressure distribution on nacelle in landing configuration ($\alpha = 6°$)

4.3 Comparison of REF2-2013 and REF3-2015 Landing Configuration

The configurational differences between the two aircraft concepts are thought to have notable influence on the high-lift performance of the aircraft. The wing sweep, the wing position, and the engine type and position are thereby thought to have the biggest impact and are therefore investigated in more detail for the landing configuration at $\alpha = 6°$.

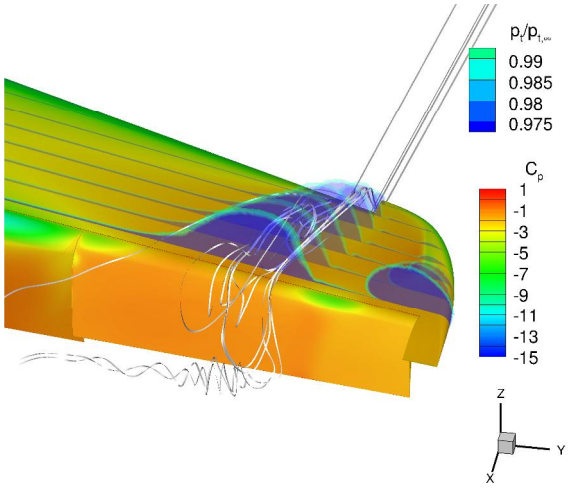

Figure 12: Total pressure loss due to side-edge vortex at the outboard wing ($\alpha = 16°$)

Figure 13 compares the jet momentum distribution along the midline of the blowing slot (solid lines) between the REF2-2013 and the REF3-2015 landing configuration. Furthermore, the figure depicts the contribution of each plenum to the total jet momentum coefficient (dash-dotted lines). The trend of both parameters is similar for both aircraft designs with the jet momentum steadily increasing along the flap from the wing root towards the outboard region as the local angle of attack and thus the momentum losses within the boundary layer increase towards the outboard region. In contrast, the C_μ values with respect to the aircraft's reference area decrease towards the outboard segments due to the decreasing local chord length and slot height. For $\eta > 0.82$, the levels of the jet momentum are considerably smaller due to the lower aileron deflection. The levels of the jet momentum and the jet momentum coefficient of the REF3-2015 are generally slightly lower compared to the ones of REF2-2013. This is expected to some extent as the higher sweep angle reduces the effective free stream velocity, which in turn leads to a reduced

demand in jet momentum. However, the magnitude of the reduction is unexpected and has to be investigated further.

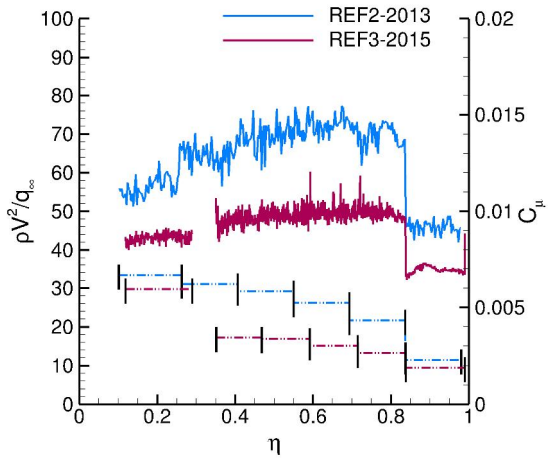

Figure 13: Comparison of the jet momentum distribution along the blowing slot (solid lines) and the contribution of each plenum to the total jet momentum coefficient (dash-dotted lines) between REF2-2013 and REF3-2015 in landing configuration

The influence of the propulsion system and its position is illustrated in figure 14, which depicts the flowfield in terms of M/M_∞ in a $Y = \text{const.}$-cutting plane at the position of the engine. For all the cases, the contour plots reveal high Mach numbers above and rather low Mach numbers below the main wing, indicating positive circulation. The engine nacelle of REF2-2013 is located in front of the main wing and thus within its upwash region (figures 14(a) and 14(b)). The lift contribution of the nacelle is therefore increased. In contrast, the nacelle of REF3-2015 is located behind the wing and is exposed to the main wing's downwash (figure 14(c)). As a result, the nacelle's lift contribution is reduced. Besides the lift contribution due to the nacelle, the engine also affects the flow conditions at the main wing. In case of REF2-2013 the flow velocity downstream of the propeller is significantly increased as shown in figure 14(b). The locally increased velocity leads to lift augmentation, which is according to the Kutta-Joukowski theorem, particularly high in conjunction with high-circulation wings. In the context of high-lift aerodynamics this type of lift augmentation is also referred to as slipstream deflection [1]. For REF3-2015 with the UHBR engine being mounted over the main wing's trailing edge, the distinct effect of thrust has not been investigated, yet. It is assumed that thrust may have a positive effect on the main wing's lift due to a reduction in pressure at the trailing edge. While this effect may be noteworthy for a take-off scenario it is expected to be rather low under landing conditions.

Figure 17 illustrates the surface pressure distribution in chordwise direction of the spanwise section at $\eta = 0.75$. Generally, the surface pressure distribution of the REF2-2013 without thrust and the REF3-2015 configuration are very similar. The suction peaks at the leading edge and trailing edge are however slightly higher on the REF3-2015 configuration. The surface pressure coefficient at the leading edge stagnation point is slightly lower on the REF3-2015 configuration due to the larger sweep angle. Furthermore, the position of the leading edge stagnation point of the REF3-2015 configuration is shifted downstream, indicating higher circulation.

Figure 16 compares the suction peak distributions along the leading edge and trailing edge at $\alpha = 6°$ between the REF2-2013 and REF3-2015 landing configurations. The suction peak distributions along the trailing edge devices (figure 16(a)) generally indicate similar trends for the REF2-2013 without thrust and the REF3-2015 configuration. The magnitude of the suction peak increases from the wing root towards the outboard flap with the maximum being slightly further outboard on the REF3-2015 configuration. On the aileron, the suction peak is obviously smaller due to the lower aileron deflection angle. The main difference between the trailing edge suction peak distributions of the two configurations is caused by the flap cutout at the pylon position ($0.28 \leq \eta \leq 0.36$) on the REF3-2015 configuration. The flap cutout leads to a reduction of the flap suction peak over a wide range of the span ($0.21 \leq \eta \leq 0.48$). Compared to REF2-2013, the trailing edge suction peak

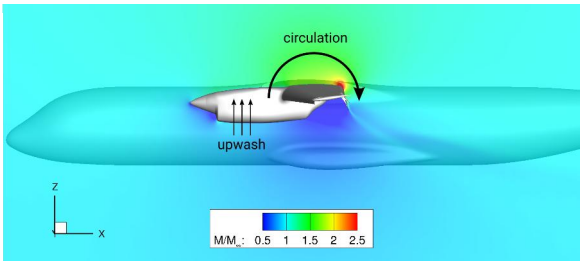

(a) REF2-2013 without thrust

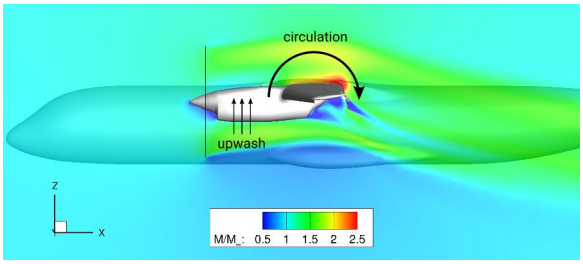

(b) REF2-2013 with thrust

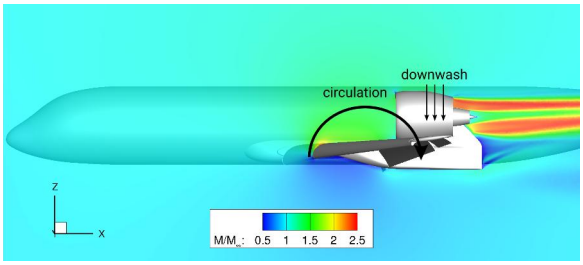

(c) REF3-2015

Figure 14: Flow conditions in Y-cutting plane at engine position for $\alpha = 6°$

of REF3-2015 is furthermore reduced in the midboard region, which may be caused by the higher wing sweep. Generally, wing sweep causes lower flap loads due to the reduced effective free stream velocity. Furthermore, the wing load is redistributed towards the wing tip in the case of positive wing sweep. In the inboard region, this effect cannot be observed as the REF2-2013 trailing edge suction peak is adversely affected by the influence of the wing-body junction. Due to the various effects, it is difficult to evaluate the exact impact of each single aspect. It is also noteworthy that the maximum of the suction peak in the

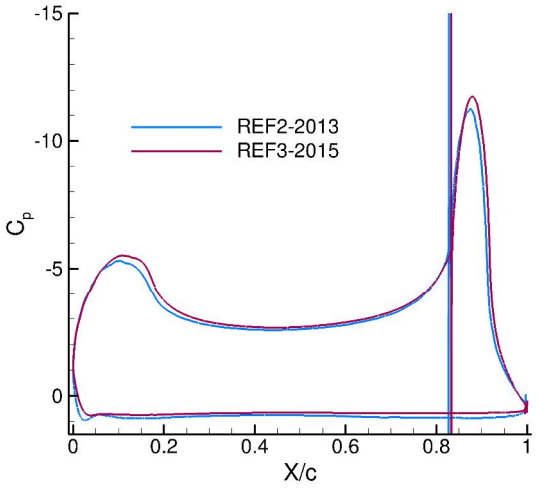

Figure 15: Comparison of surface pressure distribution in wing section at $\eta = 0.75$ between REF2-2013 without thrust and REF3-2015 landing configuration ($\alpha = 6°$)

outboard region is higher on the REF3-2015 configuration despite the larger wing sweep and the lower jet momentum (coefficient).

When thrust is applied on the REF2-2013 landing configuration, the trailing edge suction peak notably increases between $0.15 \leq \eta \leq 0.58$. The increase in the suction peak is even higher at the downwash side of the propeller (outboard of the nacelle), where the deflection of the slipstream due to the main wing (see figure 8(a)) causes further flow acceleration.

At the leading edge, the engine mounting on the REF2-2013 leads to a gap in the suction peak as figure 16(b) illustrates. The impact of the droop nose cutout in the region of the nacelle however appears to be less compared to the impact of the flap cutout on the trailing edge suction peak distribution of the REF3-2015 configuration. Besides the difference due to the nacelle, the suction peak in the inboard region is generally stronger on the REF2-2013 configuration without thrust with the difference being $\Delta C_{p,min} \approx 1$. The maximum of $|C_{p,min}|$ occurs at $\eta = 0.61$ in case of the REF2-2013 configuration. The maximum of $|C_{p,min}|$ on the REF3-2015 config-

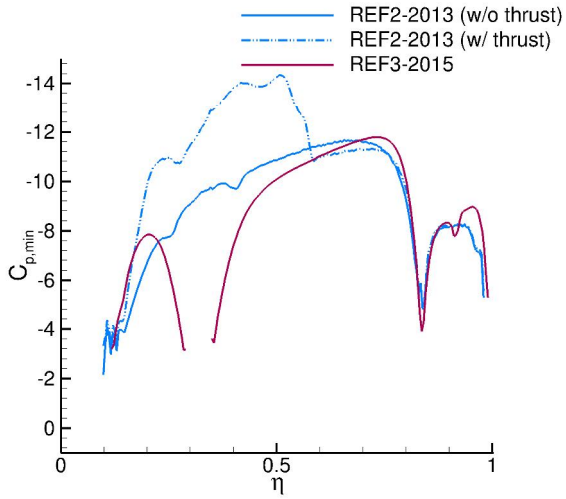

(a) Trailing edge

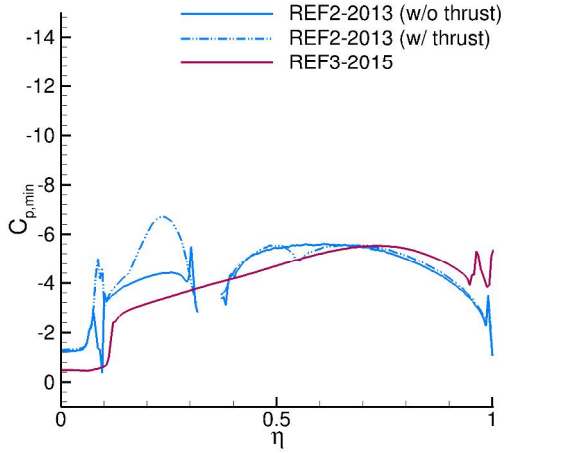

(b) Leading edge

Figure 16: Comparison of suction peak distribution along span between REF3-2015 and REF2-2013 landing configuration at $\alpha = 6°$

uration occurs slightly further outboard at $\eta = 0.74$. Both, the lower $|C_{p,min}|$ values in the inboard region and the maximum of $|C_{p,min}|$ being located further towards the wing tip on REF3-2015 are most likely connected to the higher sweep angle. As mentioned above, positive wing sweep generally causes a load shift towards the wing tip due to reduced induced angles of attack (increased local angles of attack) towards the wing tip. The leading edge suction peak is very sensitive to a change in the angle of attack and thus reflects the load shift with the suction peak on REF3-2015 being higher than on REF2-2013 in the outboard region. The spanwise distribution of the leading edge suction peak is also an indicator of regions being prone to flow separation as high leading edge suction peaks are generally accompanied by strong adverse pressure gradients. The leading edge suction peak distribution for REF3-2015 therefore confirms the tendency of outboard flow separation due to higher wing sweep (compared to REF2-2013) as seen in figure 9.

Applying thrust to the REF2-2013 configuration leads to a notable increase of the leading edge suction peak in the upwash region of the propeller inboard of the nacelle ($0.11 \leq \eta \leq 0.3$). Outboard of the nacelle, the suction peak is nearly unaffected. Here, an increase due to higher velocities of the oncoming flow is counter-acted by the effect of a reduced local angle of attack due to the downwash of the propeller.

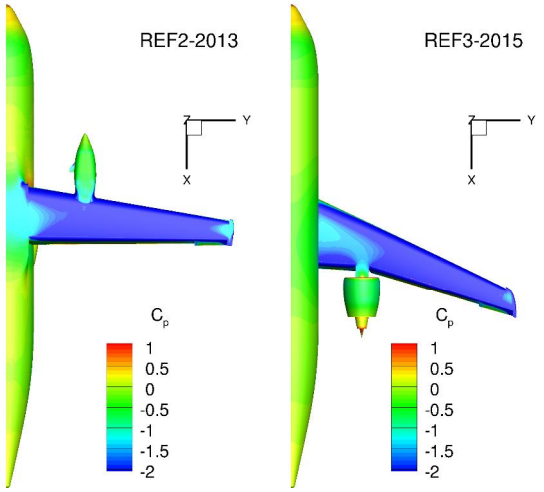

Figure 17: Comparison of surface pressure distribution between REF2-2013 (w/o thrust) and REF3-2015 landing configuration ($\alpha = 6°$)

The vertical main wing position mainly affects the surface pressure distribution of the fuselage. Figure 17 therefore compares the surface pressure of the fuselage between REF2-2013 and REF3-2015. In the case of REF2-2013 without thrust, the low pressure zone above the main wing can propagate onto the fuselage due to its high wing position, causing a low surface pressure zone on the fuselage's upper side. In contrast, the surface pressure on the upper side of the fuselage is notably higher on the REF3-2015 configuration. Here, the upper side of the fuselage is affected less by the main wing due to the low wing position.

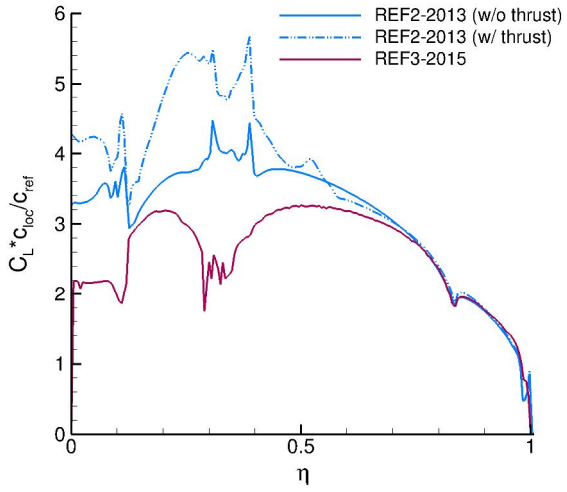

Figure 18: Comparison of lift distribution between REF2-2013 and REF3-2015 landing configuration ($\alpha = 6°$)

	$C_L\|_{REF2}$	$C_L\|_{REF3}$	$\Delta C_L\|_{REF3-REF2}$
Fuselage	0.32	0.24	−0.08
Main Wing (w/ DN)	2.13	1.93	−0.20
Flap	0.47	0.36	−0.11
Aileron	0.06	0.06	0.0
Nacelle	0.13	0.0	−0.13
Total	3.11	2.59	−0.52

Table 4: Component-wise contributions to the total lift coefficient at $\alpha = 6°$

The effects described above obviously impact the lift distribution as illustrated in figure 18. Regarding REF2-2013 without thrust and REF3-2015, the most significant differences between the lift distributions can be found in the inboard region. For $\eta \geq 0.12$, the local lift of REF2-2013 is notably higher compared to the REF3-2015 configuration due to the lower surface pressure on the fuselage's upper side. A comparison of the component-wise contributions to the total lift coefficient (table 4) yields that the fuselage of REF3-2015 contributes $\Delta C_L = -0.08$ less to the total lift coefficient compared to the one of REF2-2013. At the main wing, between $0.23 \leq \eta \leq 0.49$, the lift distribution of REF3-2015 is negatively affected by the engine integration. The flap cutout in this region is the main reason for the lift contribution from the flap being $\Delta C_L = -0.11$ lower compared to the one of REF2-2013. Furthermore, the engine nacelle does not contribute any lift as its incidence angle is significantly lowered by the main wing's downwash (see figure 11). In contrast, the nacelle of the propeller engine causes an increase in local lift on the REF2-2013 configuration and therefore contributes $C_L = 0.13$ to the total lift coefficient. Besides the effect on the lift contribution of the flap and the engine nacelle, the engine integration of the REF3-2015 landing configuration also affects the lift creation of the main wing including the droop nose, which causes the large extent of the region with reduced local lift in the lift distribution as shown in figure 18. It is however difficult to quantify this effect as other influences such as load redistribution towards the wing tip due to the wing sweep may also reduce the local lift in the

inboard region. In summary, the main wing (with droop nose) of REF3-2015 produces $\Delta C_L = -0.2$ less lift compared to the one of REF2-2013. The total lift coefficient at $\alpha = 6°$ is therefore reduced by $\Delta C_L = -0.52$.

When slipstream effects due to propeller thrust are considered on REF2-2013, the difference is even higher as the dash-dotted blue line in figure 18 and table 5 demonstrate. The velocity increase in the inboard region due to the propeller slipstream lead to an increase in the lift distribution from $0 \leq \eta \leq 0.48$. The lift increase is highest in the inboard region of the main wing due to the rotational sense of the propeller and the tapering of the main wing. The contributions to the total lift coefficient of the main wing with droop nose and the flap increase due to slipstream effects by $\Delta C_L = 0.21$ and $\Delta C_L = 0.11$, respectively. Additionally, the fuselage yields a $\Delta C_L = 0.07$ higher lift. Compared to REF3-2015, the total lift coefficient of the REF2-2013 landing configuration is $\Delta C_L = 0.93$ higher at $\alpha = 6°$ when slipstream effects are considered.

While the impact is thought to be minor, it has to be kept in mind that the different meshing approaches for REF2-2013 and REF3-2015 may affect the magnitude of the differences in the C_L values between REF3-2015 and REF2-2013.

	$C_L\|_{REF2,wT}$	$\Delta C_L\|_{REF3-REF2wT}$
Fuselage	0.39	−0.15
Main Wing (w/ DN)	2.34	−0.41
Flap	0.58	−0.22
Aileron	0.06	0.0
Nacelle	0.15	−0.15
Total	3.52	−0.93

Table 5: Component-wise contributions to the total lift coefficient of REF2-2013 with thrust at $\alpha = 6°$

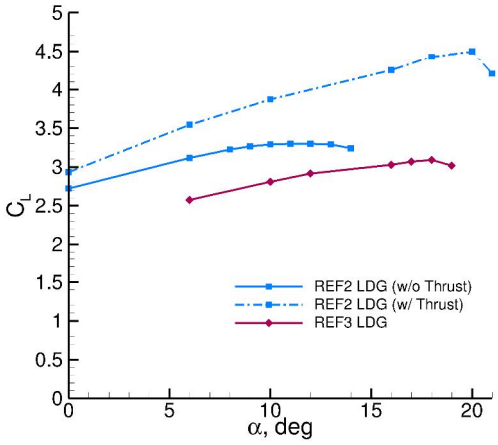

Figure 19: Comparison of lift curve between REF2-2013 and REF3-2015 landing configuration

Figure 19 compares the lift curve of the REF3-2015 landing configuration with the ones of the REF2-2013 landing configuration (with and without thrust). Compared to REF2-2013 without thrust, the REF3-2015's maximum lift coefficient of $C_{L,max} = 3.09$ is $\Delta C_{L,max} = -0.21$ lower, whereas the maximum angle of attack is increased by $\Delta\alpha = 7°$. In the case of REF2-2013, the maximum angle of attack is limited due to interaction of the nacelle vortices with the circulation control system [7]. The dash-dotted blue line indicates that the maximum lift coefficient of the REF2-2013 landing configuration is considerably increased when moderate thrust is applied. In this case, the maximum lift coefficient of the REF3-2015 configuration is $\Delta C_{L,max} = -1.40$ lower than the one of the REF2-2013 configuration. When comparing the maximum lift coefficients of REF2-2013 and REF3-2015, it has to be noted that the jet momentum coefficient of REF3-2015 is significantly lower compared to the one of REF2-2013. The analysis of the surface pressure distribution, the lift distribution, and the component-wise lift breakdown however leads to the conclusion that the lower $C_{L,max}$ of REF3-2015 compared to REF2-2013 is of fundamental nature. An increase in C_μ would furthermore lead to super

circulation and thus reduce the efficiency of the circulation control system.

4.4 REF3-2015 Take-Off Configuration

Figure 20 depicts the surface pressure distribution and skin friction lines of the REF3-2015 take-off configuration at varying angles of attack. Analogously to the landing configuration, the flow is fully attached to the main wing and the trailing edge devices at $\alpha = 6°$ (figure 20(a)). The distribution of the surface pressure coefficient indicates a reduction in the trailing edge suction peak compared to the landing configuration. At the leading edge, the suction peak in the midboard and the outboard region appears to be lower.

At $\alpha = 16°$ (figure 20(b)), the surface pressure distribution and skin friction lines indicate similar trends as seen for the landing configuration with the outer side-edge vortex causing flow separation downstream. The flow separation then propagates towards the midboard region with rising angle of attack. At $\alpha = 21.0°$ (figure 20(c)), the flow is separated from the main element for $\eta \geq 0.67$. Despite the flow being entirely attached to the flaps and the aileron, their suction peaks are strongly reduced downstream of the regions with separated flow.

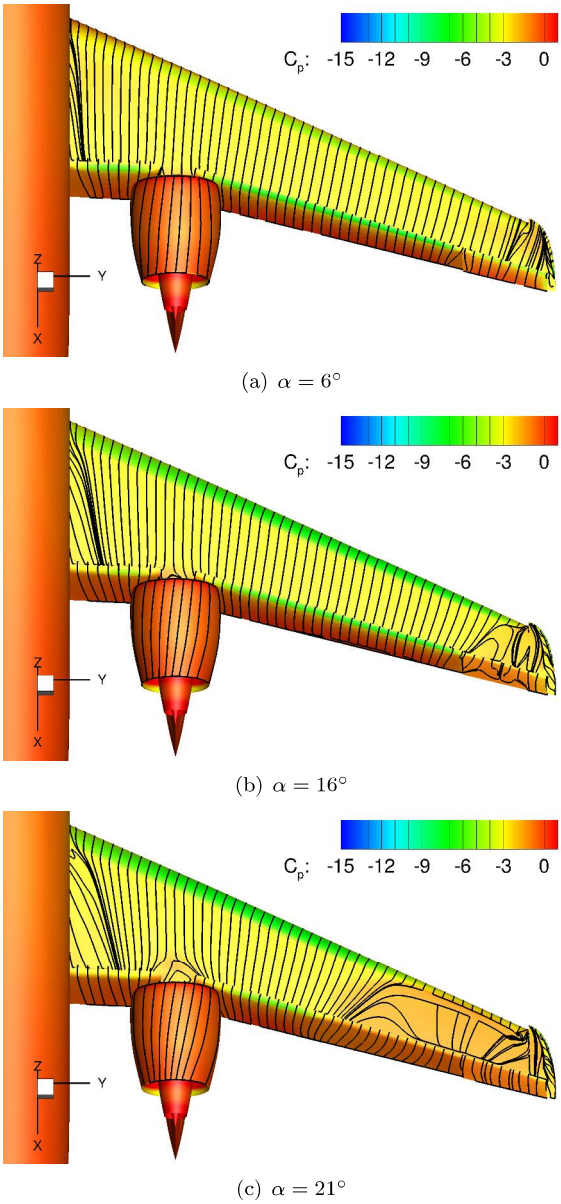

(a) $\alpha = 6°$

(b) $\alpha = 16°$

(c) $\alpha = 21°$

Figure 20: Surface pressure distribution and skin friction lines of take-off configuration at $C_\mu = 0.018$

4.4.1 Engine Intake Flow Distortion

Due to the engine's position of the REF3-2015 and the high thrust setting, the engine inlet flow is prone to distortion in take-off configuration. In contrast, the engine intake is not exposed to flow distortion in landing configuration due to rather low thrust settings. The flow conditions at the engine intake are therefore discussed for the take-off configuration only. At low and moderate angles of attack ($\alpha < 14°$), the intake flow is nearly undisturbed in take-off configuration. For $\alpha \geq 14°$, the intake flow is affected by total pressure losses from the main wing boundary layer. Figure 21(a) illustrates the near surface flow above the main wing in proximity to the engine at $\alpha = 16°$. The streamlines demonstrate that the flow in front of the engine separates from the main wing and is sucked into the engine. The total pressure of this flow is notably lower compared to the

free stream total pressure ($p_{t,\infty}$). The resulting total pressure losses at the fan plane are depicted in Figure 21(b). With rising angle of attack the total pressure losses become more severe as figure 22 illustrates for $\alpha = 19°$.

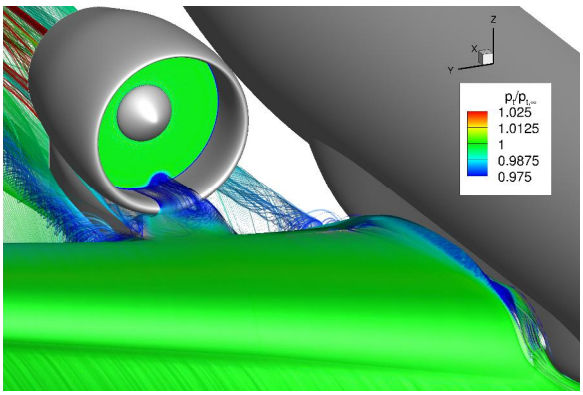

(a) Near surface streamlines visualizing main wing flow

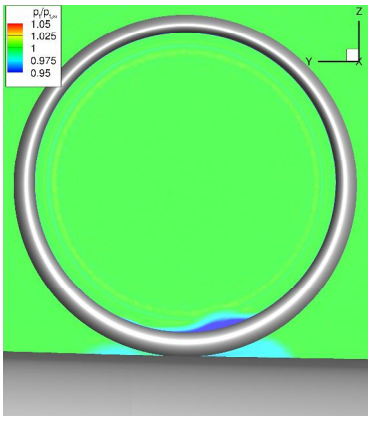

(b) Total pressure loss at fan plane

Figure 21: Flow distortion at engine intake for take-off configuration at $\alpha = 16°$

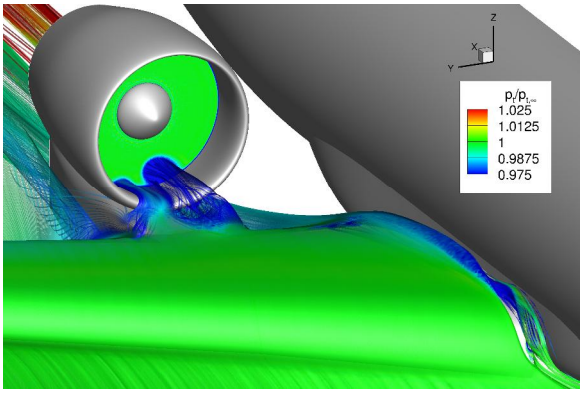

(a) Near surface streamlines visualizing main wing flow

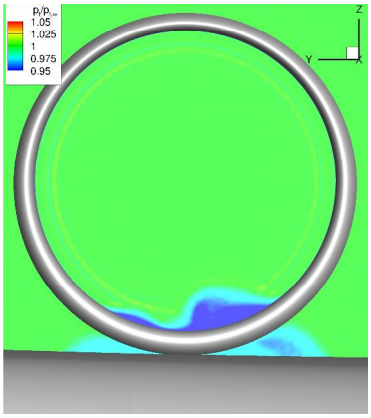

(b) Total pressure loss at fan plane

Figure 22: Flow distortion at engine intake for take-off configuration at $\alpha = 19°$

4.4.2 Comparison of Take-Off and Landing Configuration

Figure 23 compares the suction peak distributions along the span between the REF3-2015 take-off and the landing configurations. As expected, the comparison of the trailing edge suction peaks demonstrates significant lower surface pressure for the landing configuration along the entire span (figure 23(a)). At the leading edge (figure 23(b)), the suction peak of the landing configuration is stronger for $\eta > 0.4$. However, the leading edge suction peaks are nearly identical for $\eta \leq 0.4$. The reason is not fully understood as the higher flap loading due to the larger flap deflection in landing configuration is thought to increase the leading edge suction peak as well. The jet engine at the main wing trailing edge possibly affects the leading edge suction peak in this region. The influence of thrust on the REF3-2015 high-lift configura-

tions has not been investigated, yet. The phenonema can be also observed for higher angles of attack. The additional lift in landing configuration is therefore mainly produced in the midboard and outboard region of the main wing (figure 24).

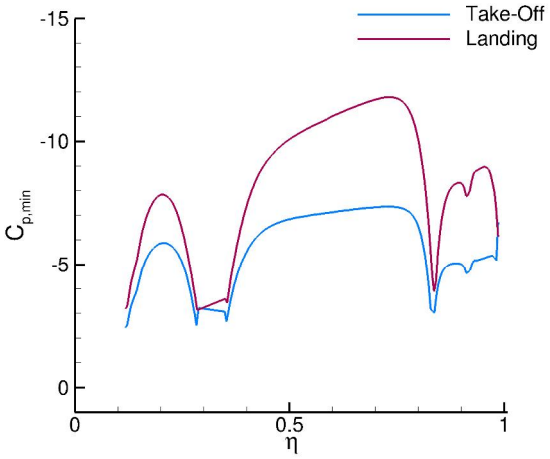

(a) Trailing edge

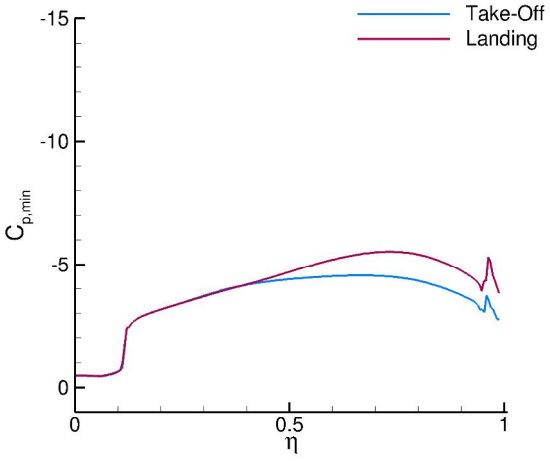

(b) Leading edge

Figure 23: Comparison of suction peak distribution along span between take-off and landing configuration at $\alpha = 6°$

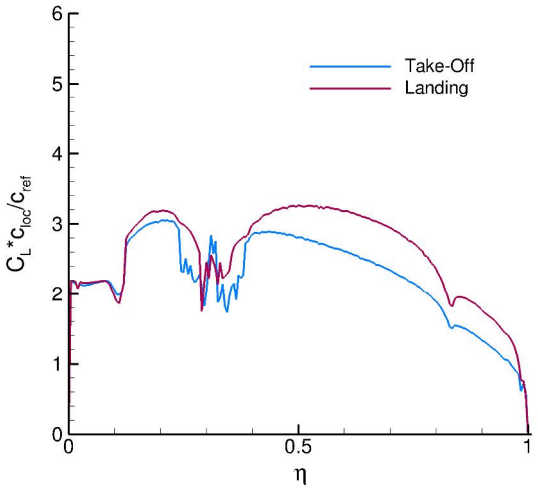

Figure 24: Comparison of lift distribution between take-off and landing configuration at $\alpha = 6°$

Figure 25 depicts the lift curves of the REF3-2015 take-off and landing configuration. Both configurations show a similar trends with the curve of the landing configuration being offset to higher levels due to the larger flap deflection. Furthermore, the lift curve slope of the landing configuration is slightly reduced compared to the one of the take-off configuration at low angles of attack. With rising angle of attack ($\alpha \geq 14°$), the lift curve slopes decrease notably due to the flow separation in the outboard region, as seen in figures 20(b) and 9(b). In take-off configuration the lift coefficient reaches $C_{L,max} = 2.90$ at a maximum angle of attack of $\alpha_{max} = 19°$ with $C_{L,max}$ being limited by flow separation in the outboard region. In landing configuration, the maximum angle of attack is lower compared to the take-off configuration with $\alpha_{max} = 17°$. The lower maximum angle of attack is most likely caused by the larger adverse pressure gradient due to the stronger suction peak in the outboard region (figure 23(b)). Despite the lower maximum angle of attack, the maximum lift coefficient is increased to $C_{L,max} = 3.09$.

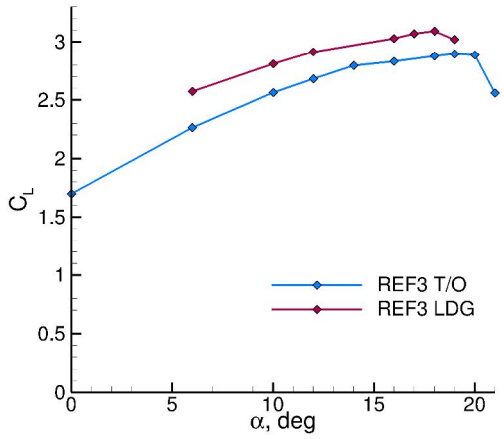

Figure 25: Comparison of lift curve between take-off and landing configuration

5 Conclusions

The results of numerical simulations of a novel transport aircraft concept (REF3-2015) with over-the-wing engines, and circulation control in take-off and landing configuration are presented. At critical jet momentum coefficient, the maximum lift coefficient yields 2.90 in take-off configuration and 3.09 in landing configuration. In both cases, the main wing stalls due to flow separation in the outboard region. The outboard flow separation is initially triggered by the side-edge vortex of the unprotected leading edge. The analysis of the leading edge suction peak distribution reveals that this region is most prone to pressure induced flow separation, which most likely promotes the propagation of flow separation at higher angles of attack.

An important aspect of this configuration is the engine position, which makes the engine inflow prone to flow distortion. An analysis of the engine inflow yields that due to the high thrust setting in take-off configuration the engine inflow is affected by total pressure losses of the main wing boundary layer at high angles of attack. In landing configuration, the engine inflow remains unaffected because of the lower thrust setting.

In order of assess the influence of configurational aspects on the high-lift performance, the REF3-2015 landing configuration is compared to the landing configuration of a high-wing low-sweep aircraft design with turbo-prop engines (REF2-2013). The comparison focused in particular on three main aspects, namely the engine/engine position, main wing sweep, and vertical position of the main wing. The following conclusions can be drawn:

- **Engine / engine position:** Depending on the engine's chord-wise position, the nacelle may be exposed to upwash or downwash of the main wing. In the case of high circulation wings, the difference can have a significant impact on the lift contribution of the nacelle. In the present investigation, the nacelle, that is positioned in front of the main wing produced $C_L = 0.13$, whereas the nacelle mounted at the trailing edge of the main wing does not produce any lift at $\alpha = 6°$. Mounting the nacelle to the trailing edge furthermore requires a flap cutout that significantly reduces the lift generation of the main wing.

  Utilizing an engine with propeller in front of the wing significantly increases the lift generation of this type of aircraft due to slipstream deflection.

- **Wing sweep:** On the one hand, wing sweep reduces the jet momentum coefficient of the circulation control system, which is necessary to achieve fully attached flaps. On the other hand, wing sweep reduces the lift generation as it reduces the effectivity of the high-lift system and causes a redistribution of the wing load. While the first is difficult to evaluate based on the present comparison, the latter is demonstrated by the suction peak distributions. The load redistribution also affects the stall behavior of the main wing. Even though it can be counter-acted by modifying the wing twist, it may become more difficult for highly swept wings to find a good compromise for the twist distribution between the cruise configuration and the high-lift configurations.

- **Wing position:** The vertical wing position affects the lift generation of the fuselage. In the case of a high wing position, the lower pressure on the upper side of the main wing can propagate onto the fuselage and therefore increase the fuselage's lift contribution. The high wing configuration therefore appears to be more favorable in terms of lift generation.

References

[1] G. K. Korbacher. Aerodynamics of powered high--lift systems. Annual Review of Fluid Mechanics, pages 319–358. 1974.

[2] R. J. Englar, G. M. Blaylock, and R. J. Gaeta. Recent Experimental Development of Circulation Control Airfoils and Pneumatic Powered-Lift Systems. AIAA Paper 2010-345, AIAA, 2010.

[3] C. Jensch, K.C. Pfingsten, R. Radespiel, M. Schuermann, M. Haupt, and S. Bauss. Design aspects of a gapless high-lift system with active blowing. Aachen, Germany, 2009. Proceedings Deutscher Luft- und Raumfahrtkongress.

[4] D. D. Marshall and K. K. Jameson. Overview of Recent Circulation Control Modeling Activities at Cal Poly. Orlando, USA, 2010. American Institute of Aeronautics and Astronautics.

[5] D. Keller and R. Rudnik. Numerical Investigation of Engine Effects on a Transport Aircraft with Circulation Control. *Journal of Aircraft*, 52(2):421–438, 2015.

[6] D. Keller and R. Rudnik. Numerical Investigations of Aerodynamic Properties of a Propeller Blown Circulation Control System on a High Wing Aircraft. *CEAS Aeronautical Journal*, 7(3):441–454, 2016.

[7] D. Keller, Y. J. Hasan, and R. Rudnik. Nacelle strake design for short takeoff and landing configuration with turboprop engines. *Journal of Aircraft*, 55(6):2444–2453, 2018.

[8] D. Keller and R. Rudnik. Investigation and improvement of directional stability and control of a propeller-driven stol aircraft. *CEAS Aeronautical Journal*, 10(3):909–924, Sep 2019.

[9] L. Savoni, R. Rudnik, and A. Ronzheimer. High Lift Design and Aerodynamic Assessment for an Over-the-Wing Pylon-Mounted Engine Configuration with STOL Capabilities. Number 2018-4207, Atlanta, Georgia, USA, 2018. American Institute of Aeronautics and Astronautics.

[10] T. Gerhold. Overview of the Hybrid RANS Code TAU. In *MEGAFLOW – Numerical Flow Simulation for Aircraft Design*, volume 89 of *Notes on Numerical Fluid Mechanics and Multidisciplinary Design*, pages 81–92. Springer, 2005.

[11] P.R. Spalart and S.R. Allmaras. A One–Equation Turbulence Model for Aerodynamic–Flows. AIAA Paper 92–439, 1992.

[12] P.R. Spalart and M. Shur. On the sensitization of turbulence models to rotation and curvature. volume 1 of *Aerospace Science and Technology*, pages 297–302. 1997.

[13] M. J. Churchfield and G. A. Blaisdell. Numerical Simulations of a Wingtip Vortex in the Near Field. *Journal of Aircraft*, 46(1):230–243, 2009.

[14] K. C. Pfingsten, C. Jensch, K. W. Körber, and R. Radespiel. Numerical Simulation of the Flow Around Circulation Control Airfoils. In *First CEAS European Air and Space Conference*, Berlin, Germany, 2007.

[15] K. C. Pfingsten and R. Radespiel. Experimental and Numerical Investigation of a Circulation Control Airfoil. In *47th AIAA Aerospace Sciences Meeting*, number AIAA-2009-0533, Orlando,Florida, 2009.

[16] W. Heinze, C. M. Österheld, and P. Horst. Multidisziplinäres Flugzeugentwurfsverfahren PrADO - Programmentwurf und Anwendung im Rahmen von Flugzeug-Konzeptstudien.

In Deutsche Gesellschaft für Luft-und Raumfahrt (DGLR), editor, *DGLR-Jahrbuch 2001*, volume 3, pages 1701–1712. Bonn, 2001.

[17] Daniel Giesecke, Marcel Lehmler, Jens Friedrichs, Jason Blinstrub, Lothar Bertsch, and Wolfgang Heinze. Evaluation of ultra-high bypass ratio engines for an over-wing aircraft configuration. *Journal of the Global Power and Propulsion Society*, 2:493–515, 10 2018.

[18] D. Keller. Numerical Approach Aspects for the Investigation of the Longitudinal Static Stability of a Transport Aircraft with Circulation Control. In *New Results in Numerical and Experimental Fluid Mechanics IX*, volume 124 of *Notes on Numerical Fluid Mechanics and Multidisciplinary Design*, pages 13–22. Springer, 2014.

[19] M. Burnazzi and R. Radespiel. Design and Analysis of a Droop Nose for Coanda Flap Applications. *Journal of Aircraft*, 51(5):1567–1579, 2014.

[20] CentaurSoft. Centaur hybrid grid generation system. In [online web site], URL: http://www.centaursoft.com. [retrieved 19th November 2012].

[21] M. Leatham, S. Stokes, J. Shaw, J. Cooper, J. Appa, and T. Blaylock. *Automatic mesh generation for rapid-response Navier-Stokes calculations.*

[22] Ralf Rudnik, Stefan Melber-Wilkending, and Peter Risley-Settle. *TAU-SOLAR Contributions to the 3rd High Lift Prediction Workshop.*